Shear crack kinematics in reinforced engineered cementitious composite (ECC) beams

Gu, Dawei; Xu, Haowen; Huang, Yitao; Zhu, Yusen; Pan, Jinlong; Luković, Mladena

DOI
10.1016/j.cscm.2024.e03587

Publication date
2024

Document Version
Final published version

Published in
Case Studies in Construction Materials

Citation (APA)
Gu, D., Xu, H., Huang, Y., Zhu, Y., Pan, J., & Luković, M. (2024). Shear crack kinematics in reinforced engineered cementitious composite (ECC) beams. *Case Studies in Construction Materials*, *21*, Article e03587. https://doi.org/10.1016/j.cscm.2024.e03587

Case Studies in Construction Materials 21 (2024) e03587

Contents lists available at ScienceDirect

Case Studies in Construction Materials

journal homepage: www.elsevier.com/locate/cscm

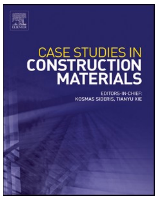

Shear crack kinematics in reinforced engineered cementitious composite (ECC) beams

Dawei Gu [a], Haowen Xu [a], Yitao Huang [b], Yusen Zhu [a], Jinlong Pan [a,*], Mladena Luković [b]

[a] School of Civil Engineering, Southeast University, Nanjing, China
[b] Faculty of Civil Engineering and Geosciences, Delft University of Technology, Delft, the Netherlands

ARTICLE INFO

Keywords:
Engineered cementitious composite (ECC)
Strain-hardening cementitious composite (SHCC)
Shear
Critical Shear Crack (CSC)
Digital image correlation (DIC)

ABSTRACT

The fiber's bridging effect across the shear cracks is considered to play an important role of resisting shear in engineered cementitious composite (ECC), and fiber reinforced material in general. To quantify the shear crack kinematics (i.e., shear crack opening and sliding displacements) in reinforced ECC (R/ECC) beams, a crack measuring algorithm based on the full-field displacement spectrum is developed by using the Digital Image Correlation (DIC) technology. In addition, a novel distributed strain-measuring methodology was used to detect the strain distribution along the transverse and longitudinal reinforcement. Reinforced beams made of traditional concrete (R/C) and mortar (R/M) were used as reference. Through aforementioned monitoring schemes, the role of matrix (V_c) and stirrups (V_s) in shear resistance mechanism could be independently understood and evaluated. The R/ECC beams exhibited much higher V_c than the reference reinforced concrete (R/C) beams (by 68%~104%). Nevertheless, the shear crack measuring results revealed that the higher shear strength in R/ECC did not always result from the fiber's bridging effect across the critical shear crack (CSC) but of high shear-resisting contribution from ECC in shear-compression zone. For a better understanding of the shear failure mechanisms, phenomenological models of shear crack kinematics in R/C and R/ECC beams are proposed.

1. Introduction

Engineered cementitious composite (ECC), also named as strain-hardening cementitious composite (SHCC), is a new type of cement-based material which can exhibit strain-hardening and multiple cracking behavior under tension by incorporating usually 1% ~ 2% of synthetic fiber. Different from normal concrete, the crack in ECC can be bridged by short random fibers, followed by their two-way pull-out behavior and allowing the further increase of load [1,2]. Before reaching the tensile strength of fibers, the cementitious matrix would fracture and new crack could form. To realize the featured steady-state and multiple cracking in ECC, the strength criterion for crack initiation and the energy criterion for flat crack propagation should be met by carefully tailoring the mechanical properties of fiber, matrix and fiber-matrix bond [3]. Generally, higher maximum complimentary energy but lower toughness of the matrix material at the crack tip and lower cracking strength are desirable in the material design of ECC. Therefore, artificial flaws and high volumes of inert filler (e.g., fly ash, cenosphere, limestone powder and silica fume) are often incorporated in the matrix [4,5]. Benefit from this, ECC can exhibit an ultimate tensile strain over 3%, which is 300 times higher than that of concrete. During the last

---

* Corresponding author.
E-mail address: cejlpan@seu.edu.cn (J. Pan).

https://doi.org/10.1016/j.cscm.2024.e03587
Received 3 June 2024; Received in revised form 9 July 2024; Accepted 29 July 2024
Available online 30 July 2024

decades, various types of functional, eco-friendly and ultra-high performance ECC have been developed, providing promising solutions to address the safety, durability and sustainability issues of infrastructures [6–12].

When subjected to shear, ECC shows significantly higher strength, ductility and energy dissipation than normal concrete [13,14]. Owing to its superior shear performance, ECC has been successfully used in shear-critical structural elements (e.g., shear coupling beams in high-rise buildings [15–17], shear walls [18,19], columns [20,21], beam-column joints [22–24], etc.) and shear strengthening of existing concrete structures [25–27]. Generally, the shear carrying capacity (V_u) of reinforced concrete (R/C) or reinforced ECC (R/ECC) beams can be categorized into two components: shear resistance from matrix (V_c) and stirrups (V_s), as shown in Fig. 1. The V_s can be rewritten as $\sum_1^n V_{si}$, where V_{si} is the tensile force of *i*th stirrup crossed by the critical shear crack (CSC), and *n* is the number of crossed stirrups, as described by Eq. (1). Obviously, the V_s can be directly quantified through measuring the stirrup strain, and then V_c can be obtained by subtracting V_s from V_u. In previous experimental work, V_s was often evaluated by using the stirrup strain measured at its half-height [28–31]. However, in reality, the CSC could intersect the stirrup at different heights, so depending on the distance from the crack and the matrix-stirrup bond, the measured strain might significantly underestimate the actual strain, and thereby the real contribution of stirrups. Considering the randomness of shear cracking path, the full-length strain distribution measurement along the stirrup seems the only solution to accurately quantify V_s and V_c [32,33].

$$V_u = V_c + V_s = V_c + \sum_1^n V_{si} \tag{1}$$

Compared to reinforced concrete (R/C) beams, a higher shear carrying capacity is commonly observed in reinforced ECC (R/ECC) beams, which is often regarded as an additional contribution from the fiber's bridging effect across the dominant shear cracks [17,29, 34,35]. Such conclusion has also been embedded in some existing shear design codes of R/ECC, in which the residual tensile stress originating from fiber bridging effect (σ_{fiber} in Fig. 1) is considered in predicting V_c [36,37]. However, limited evidence has been delivered in quantifying the shear contribution of fibers (V_f) in R/ECC beams. Recently, several experimental and analytical studies have been conducted with R/ECC [38–40] to establish a relationship between σ_{fiber} and shear crack kinematics (combined crack opening and sliding displacements), which made the quantification of V_f possible.

In this research the shear behavior of R/C, R/ECC and R/M (i.e., reinforced mortar) beams was investigated through four-point bending tests. A novel distributed strain-measuring methodology was adopted to obtain the full-length strain distribution along the transverse and longitudinal reinforcement, through which V_c and V_s could be accurately calculated. In addition, the shear crack kinematics was quantified based on the Digital Image Correlation (DIC) technology, allowing a deeper understanding of shear-resisting mechanisms in R/C, R/ECC and R/M.

2. Experimental program

2.1. Material preparation

Table 1 shows the mix proportion of different matrix materials (concrete, ECC and mortar) used in the current research. The chemical composition and particle size distribution of cement, fly ash, cenosphere, silica fume and silica sand determined by X-ray fluorescence (XRF) spectroscopy and laser particle size analyzer are shown in Table 2 and Fig. 2, respectively. The PVA fiber RECS15 developed by Kuraray Co., Ltd. was incorporated in ECC, and the detailed properties are listed in Table 3. The mortar had the same mixture as ECC except that no fiber was added. At least six cylinders with diameter of 100 mm and height of 200 mm were prepared to measure the compressive strength of concrete, ECC and mortar which were cast simultaneously with beams, following the standard ASTM C 39 [41]. Four dumbbell-shaped specimens were also fabricated simultaneously with beams to determine the tensile behavior of ECC, following the standard JC/T 2461-2018 [42].

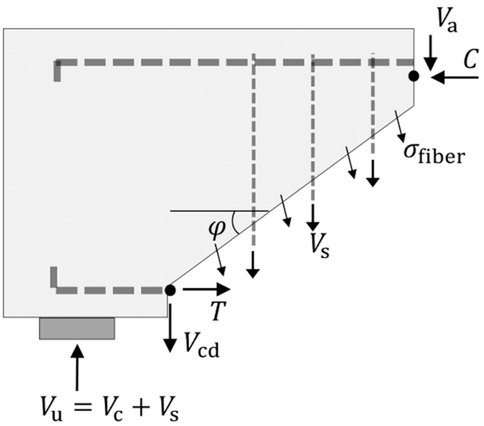

Fig. 1. Shear-resisting components in R/ECC beams.

Table 1
Mixture proportion of concrete, ECC and mortar (kg/m^3).

	C	FA	CS	SF	S	CA	W	F	SP	HPMC
Concrete	584	–	–	31	596	1064	185	–	0.5	–
ECC	426	647	162	43	256	–	332	26.8	1.6	0.5
Mortar	426	647	162	43	256	–	332	–	1.6	0.5

Note: C is cement; FA is fly ash; CS is cenosphere; SF is Silica fume; S is sand (0-5 mm); CA is coarse aggregate (5-20 mm); W is water; F is short PVA fiber; SP is superplasticizer; HPMC is hydroxypropyl methyl cellulose.

Table 2
Chemical composition of raw materials (%).

	CaO	SiO_2	Al_2O_3	SO_3	Fe_2O_3	MgO	K_2O	Na_2O	TiO_2	P_2O_5
C	56.65	20.45	6.30	3.36	3.18	1.59	0.85	0.32	0.31	0.16
FA	5.30	35.88	37.65	1.01	5.22	1.21	0.66	0.14	1.46	0.60
CS	1.96	36.33	28.83	0.63	2.85	0.48	0.70	0.32	1.22	0.39
SF	0.24	83.82	0.19	1.24	0.05	0.27	0.32	0.79	0.01	0.13

Note: C is cement; FA is fly ash; CS is cenosphere; SF is Silica fume.

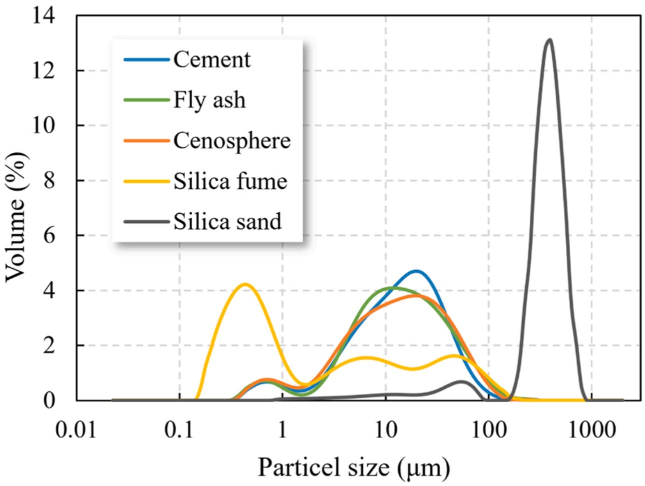

Fig. 2. Particle size distribution of raw materials in ECC.

Table 3
Details of PVA fiber incorporated in ECC.

Length (mm)	Diameter (μm)	Tensile strength (MPa)	Elastic modulus (GPa)	Ultimate tensile strain (%)
12	40	1560	41	7.5

Note: Above data are provided by the fiber producer Kuraray Co., Ltd.

All specimens for material properties characterization were made at the same day as beams, and cured under the same environmental conditions. The steel reinforcement HRB600E and HRB400E, with a diameter of 22 mm and 12 mm, respectively, were used as longitudinal and transverse reinforcement. Direct tensile tests were conducted to obtain the stress-strain relationship of steel reinforcement, following the standard GB/T 228.1-2010 [43].

2.2. Distributed strain-measuring system along steel reinforcement

To evaluate the relationship between strain distribution of stirrups and shear crack propagation, a novel distributed strain-measuring system was used. The stirrup legs were split into two halves, making cavities inside and continuously attaching ten strain gauges along the beam height (step 1 in Fig. 3). Then, the split bars were re-joined by high strength epoxy resin and mechanical tightening rings (step 2 in Fig. 3). After 72 hours of healing, the tightening rings were removed and two intact stirrup legs were connected to U-shaped bars by nuts (step 3 in Fig. 3). Finally, the closed stirrup with distributed strain gauges inside its legs were made. By using such strain measurement scheme, the strain distribution along the height of stirrup could be obtained without influencing the

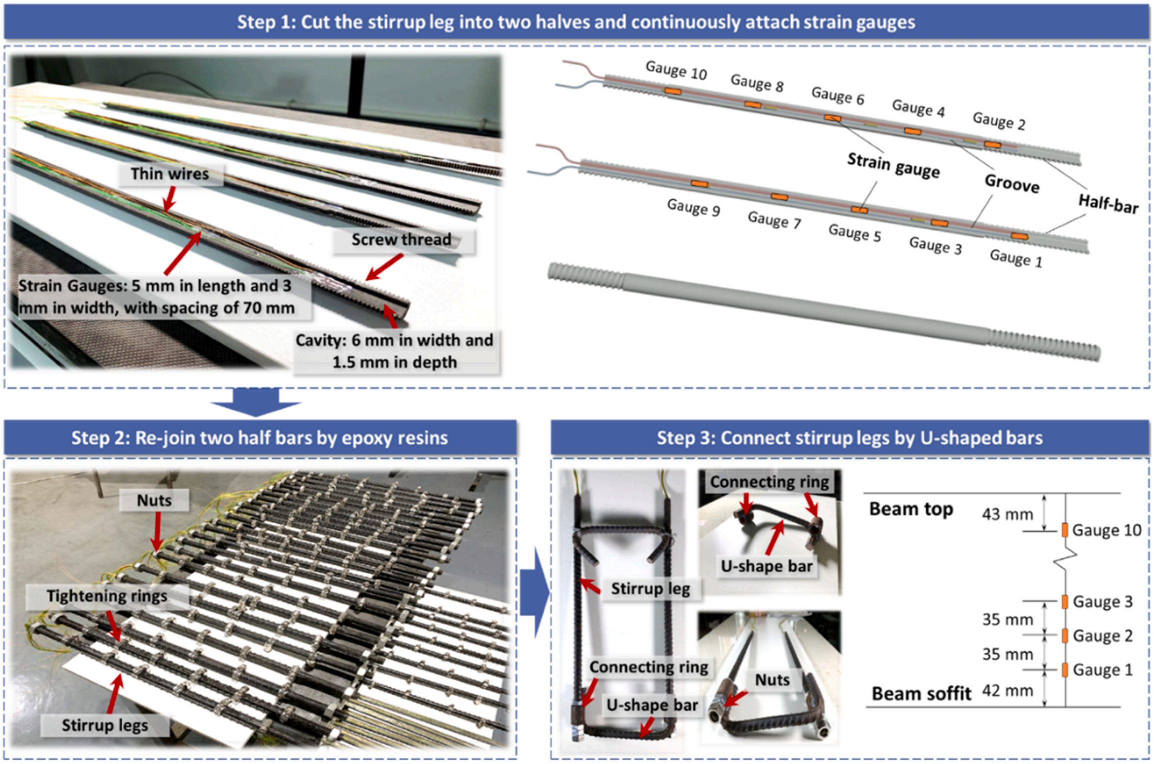

Fig. 3. Fabrication of stirrups with distributed strain gauging system.

bond between reinforcement and matrix. Similar method was also applied along the longitudinal reinforcement, where ten strain gauges were continuously arranged from the support to the mid-span (Fig. 4).

2.3. Beam specimens

Six beam specimens were fabricated for shear testing including two R/C beams, two R/ECC beams and two R/M beams with different stirrup ratios (0% and 0.38%). In this study, the concrete, ECC and mortar beams with no stirrups are named as R/C-N, R/E-N and R/M-N respectively, whereas R/C-S, R/E-S and R/M-S represent those beams with stirrups. Fig. 5 shows the specimen dimension and reinforcement details. For all beams, the right span was configured with heavy stirrups and therefore, shear failure was expected to happen only in the left span, within which the aforementioned continuous strain gauging system was employed (Fig. 6a). Considering the possible strain variation along the reinforcement cross-section caused by bending [32,44], the groove with strain gauges was made along the side of beams to measure the axial strain of reinforcement (Fig. 6b). A set of steel plates were fixed at the ends of

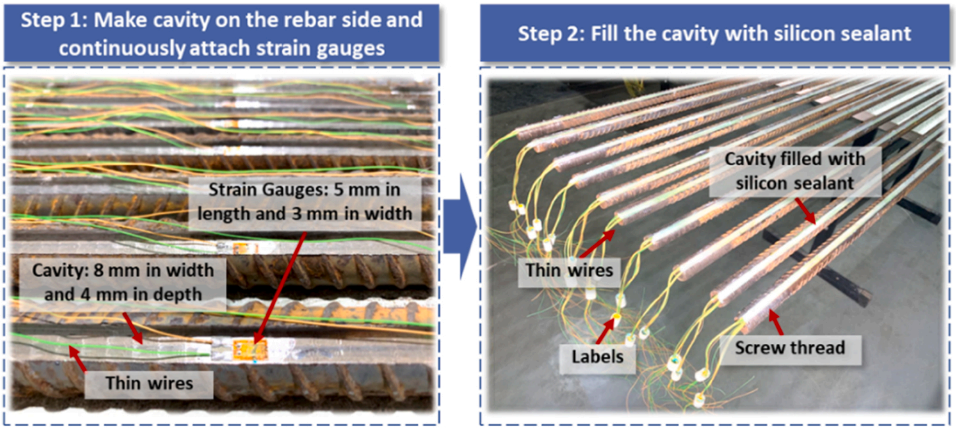

Fig. 4. Fabrication of longitudinal reinforcement with distributed strain gauging system [34].

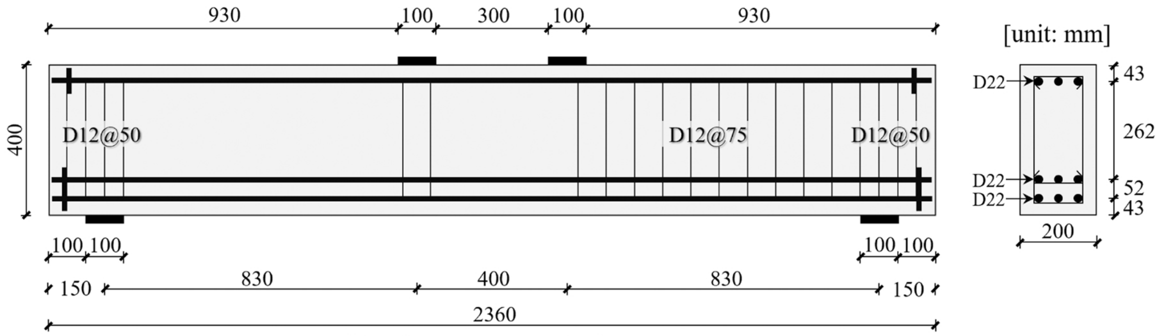

(a) R/C-N, R/E-N and R/M-N

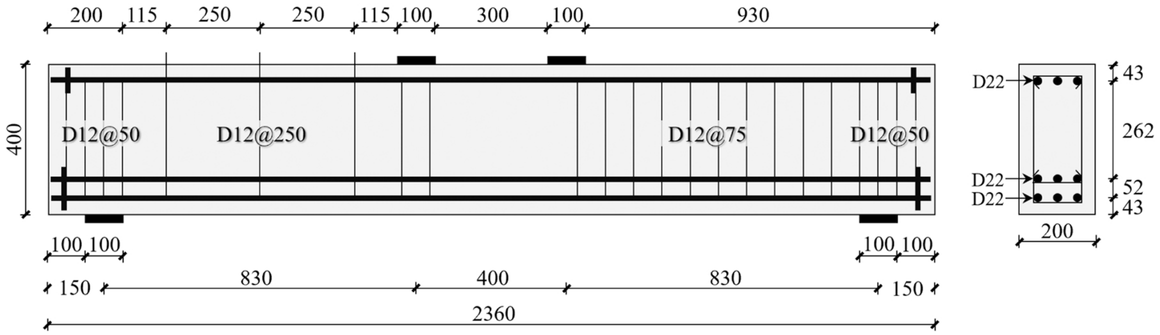

(b) R/C-S, R/E-S and R/M-S

Fig. 5. Specimen dimension and reinforcement details for: (a) beams with no stirrups; (b) beams with stirrups.

reinforcement to prevent undesired anchorage failure (Fig. 6c). After the installation and placement of the steel cage, the matrix material was poured from the sides of the beam (Fig. 6d).

2.4. Test setup

The beams were loaded under four-point bending, and the three-dimensional DIC system was equipped to detect the full

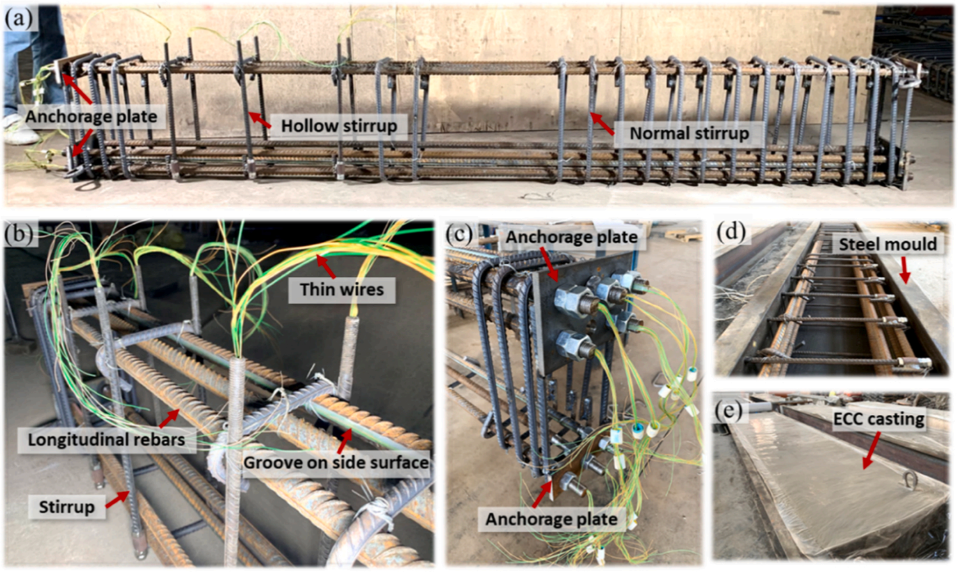

Fig. 6. Fabrication of beam specimens: (a) typical reinforcement cage; (b) reinforcement strain-gauging system; (c) reinforcement anchorage; (d) steel mould; (e) beam casting.

displacement and strain spectrum of the left span of beams, where the shear failure was expected to occur (Fig. 7). Two industrial cameras with 2048 by 2048 pixels were employed to capture images with a resolution of 0.58 mm/pixel, and the software PMLAB [45] was used for the full-field displacement and strain analysis. The accuracy of displacement detection is claimed to be 0.02 pixel, that is, 0.01 mm in this study [46]. A group of displacement transducers were used to measure the beam's deflection and potential support movement. The detected displacement and strain were recorded by several data loggers, with a recording frequency of 2 Hz. After sensors were prepared, the concentrated load was applied through displacement-controlling scheme (0.4 mm per minute).

3. Experimental results

3.1. Material tests

The compressive strength for concrete, ECC and mortar, and tensile strength and ultimate tensile strain for ECC are listed in Table 4. The tested stress-strain curves of dumbbell-shaped samples are shown in Fig. 8(a), which exhibited a unique strain-hardening behavior under uniaxial tension. The tensile behavior of steel bars used as longitudinal reinforcement (D22) and stirrups (D12) was also tested, as shown in Fig. 8(b). It can be seen that fabrication of cavities or grooves would not obviously influence the mechanical behavior of steel reinforcement as the re-joined reinforcement has nearly the same tensile response as original reinforcement.

3.2. Load-deflection response and failure mode

All six beams exhibited a shear-compression failure mode, as shown in Fig. 9, in which the shear strength was reached when the matrix crushed in shear-compression zone. The shear force-deflection relationships of six beams are plotted in Fig. 10. Generally, the R/ECC and R/M beams exhibited lower initial stiffness compared with R/C beams, which could be attributed to the lower elastic modulus and potential shrinkage cracking of ECC and mortar. As expected, the stirrups did not affect the initial stiffness of beams. To compare the shear carrying capacity, the nominal shear strength v_u, which is defined as V_u/bd (V_u is the peak shear load, b and d represent the width and effective depth of cross-section of a beam), is listed in Table 4. For the beams without stirrup, R/ECC exhibited shear strength increase by 68% and 100% compared to R/C and R/M. However, once stirrups were embedded, this increase is only 17% and 78% respectively. It revealed that the shear transfer mechanism was fundamentally altered when transverse reinforcement was embedded, which would be further discussed by separating the contribution from different shear-resisting components in Section 4.

3.3. Crack propagation

The principal strain contours of beams detected by the DIC at selected loading levels are shown in Fig. 11. Cracks can be recognized at locations of high tensile strain concentration. The initiation, propagation and branching of the CSC are conceptionally illustrated in Fig. 12.

For all beams, flexural cracks first appeared within the pure-bending region where the maximum bending moment occurred. As the applied load continued to increase, more flexural cracks could be observed along the shear span and gradually tended to rotate towards the loading point, which could be regarded as the initiation of diagonal shear cracks. At certain bending moment, splitting tensile crack along the bottom tensile reinforcement could appear as a branch of an inclined shear crack. Afterwards, a critical shear crack formed and could further propagate to both loading and supporting plates until a beam fails. Compared with R/C beams, two R/ECC beams exhibited more shear cracks within the shear span, and the addition of stirrups effectively retarded the formation of CSC.

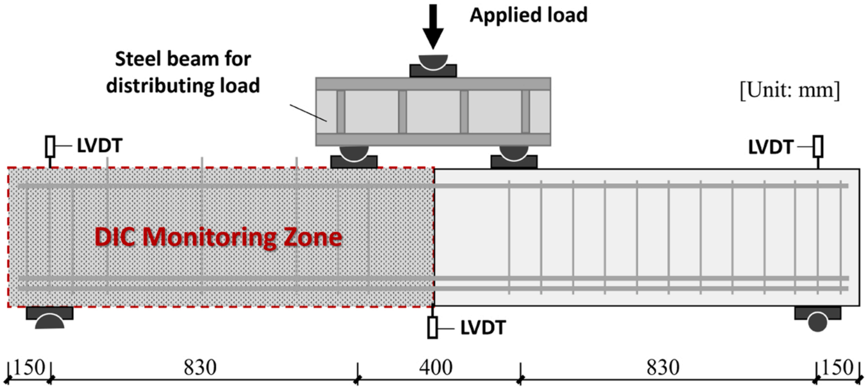

Fig. 7. Schematic diagram of experimental setup.

Table 4
Summary of beams' details and experimental results.

Specimen	Matrix	ρ_t (%)	Curing age (days)	f_c' (MPa)	f_{tu} (MPa)	ε_{tu} (%)	$V_{y,1}$ (kN)	$V_{y,2}$ (kN)	V_u (kN)	v_u (MPa)
R/C-N	Concrete	0.00	66	56.6	–	–	–	–	172.7	2.6
R/C-S	Concrete	0.38	86	53.0	–	–	187.7	288.9	359.8	5.4
R/E-N	ECC	0.00	85	56.4	8.0	3.5	–	–	289.5	4.4
R/E-S	ECC	0.38	100	54.7	7.5	3.8	343.5	415.5	421.4	6.4
R/M-N	Mortar	0.00	70	55.4	–	–	–	–	144.4	2.2
R/M-S	Mortar	0.38	86	60.2	–	–	168.2	227.5	236.6	3.6

Notes: f_c' = compressive strength; f_{tu} = tensile strength; ε_{tu} = ultimate tensile strain; ρ_t = stirrup ratio; $V_{y,1}$ = shear load at which first stirrup leg yielded; $V_{y,2}$ = shear load at which last stirrup leg yielded; V_u = peak shear load; v_u = nominal shear strength.

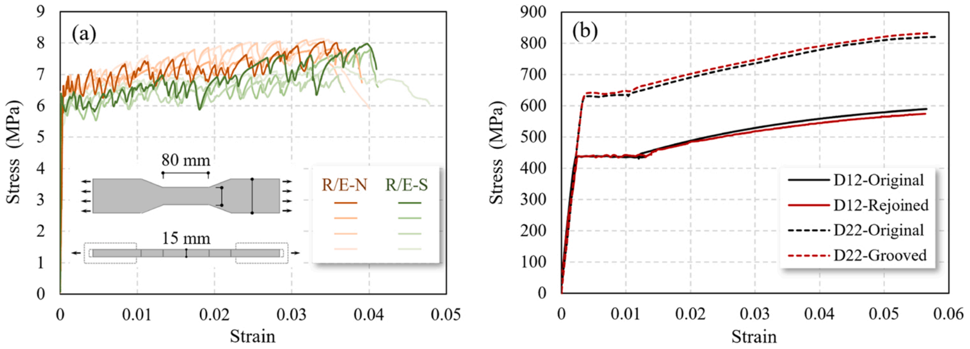

Fig. 8. Uniaxial tensile stress-strain curves of: (a) ECC; (b) steel reinforcement.

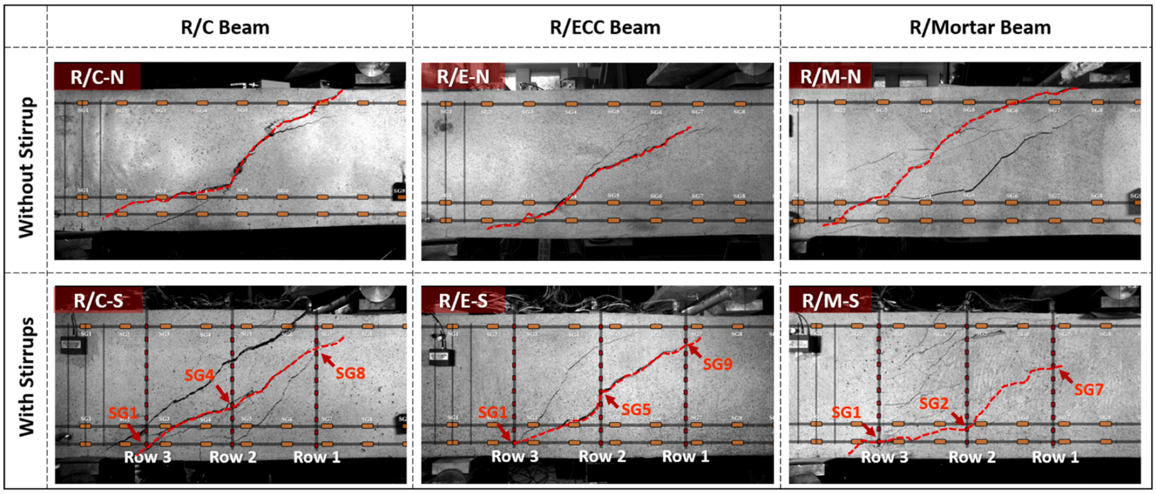

Fig. 9. Crack pattern of tested beams at ultimate failure (the red dashed line represents the CSC; 'SG' represents the strain gauge crossed by the CSC).

3.4. *Strain distribution along steel reinforcement*

Through the distributed strain-measuring system along the steel reinforcement, the full-length strain distribution along stirrups and longitudinal rebars could be obtained. The labels of stirrup legs are shown in Fig. 13, and their strain distribution at selected loading levels is exhibited in Fig. 14 to Fig. 16. Obviously, the strain distribution along stirrup legs was not uniform, and strain concentration could be always found at the location crossed by the shear cracks. Besides, not all the stirrups crossed by the CSC would yield at the peak load, for example, the strain gauging point SG9 at stirrup Row1 (stirrup leg 01 and 02) in R/E-S (Fig. 15 a and b). It reveals that the classic assumption of "all stirrups can yield" in most codes could cause an overestimation of V_s. The average strain distribution

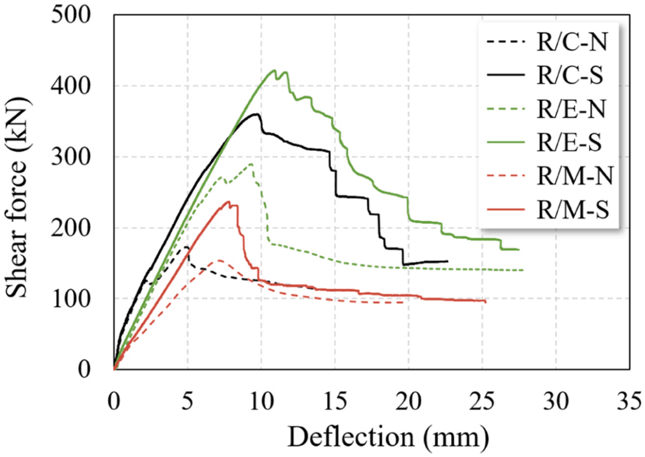

Fig. 10. Shear force-deflection curves of all six beams.

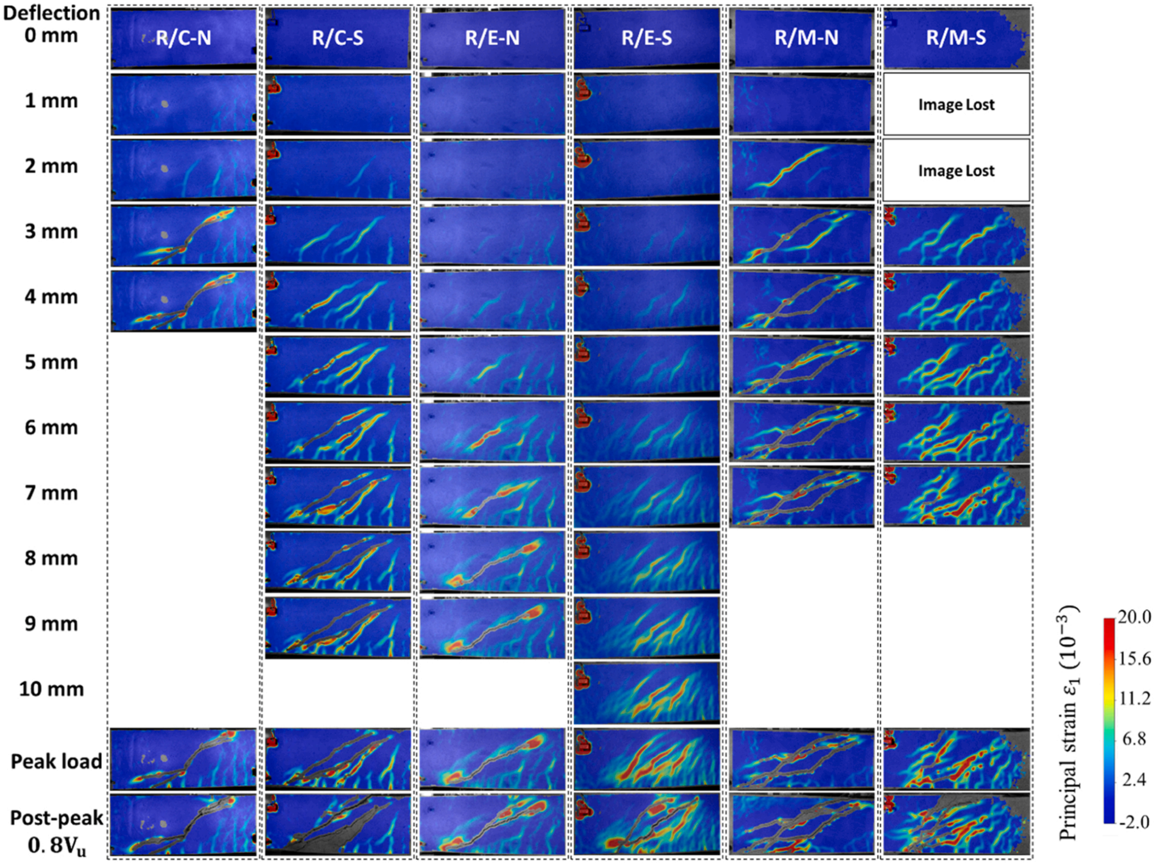

Fig. 11. Principal strain spectrum at selected loading levels for all tested beams.

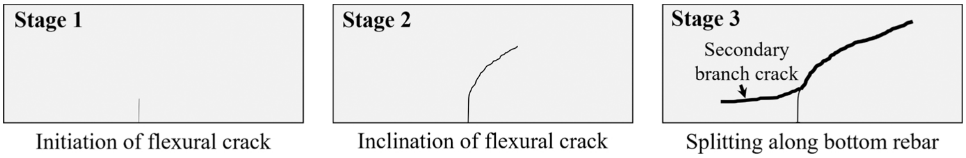

Fig. 12. Initiation, propagation and branching of the critical shear crack (CSC).

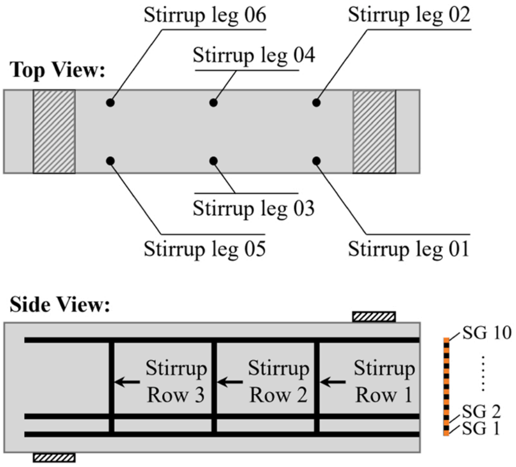

Fig. 13. Schematic diagram of the stirrup legs' ID.

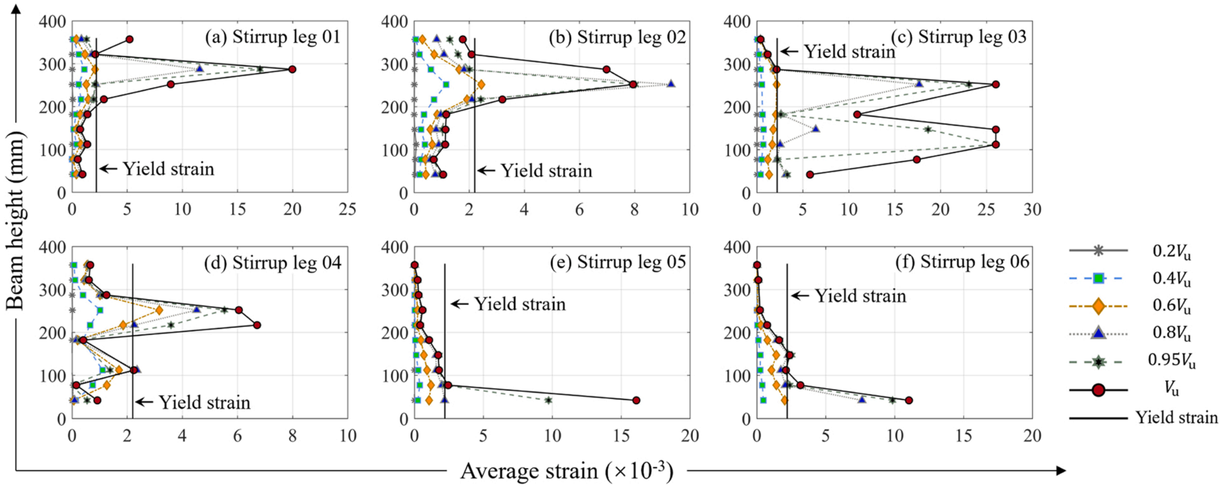

Fig. 14. Strain measurements along stirrups at selected loading levels in R/C-S.

along the bottom rebar of inner layer under selected loading levels is plotted in Fig. 17. It can be seen that the strain distribution did not follow the moment diagram when the shear crack appeared, which can be recognized as the tension-shifting effect as defined by [47].

4. Discussions

4.1. Quantification of shear crack kinematics: crack opening and sliding displacements

Through the use of DIC system, the full-field displacements of beam's surface were obtained. Furthermore, the shear crack kinematics (i.e., shear crack opening and sliding displacements) can be determined according to the following procedures (Fig. 18a): select two calculation points A and B across the shear crack, and denote their updated positions as A′ and B′ after the beam's deformation; then, the shear crack opening ω and sliding Δ can be calculated by a vector operation of $\overrightarrow{AB}$ and $\overrightarrow{A'B'}$, as expressed by Eqs. (2) and (3).

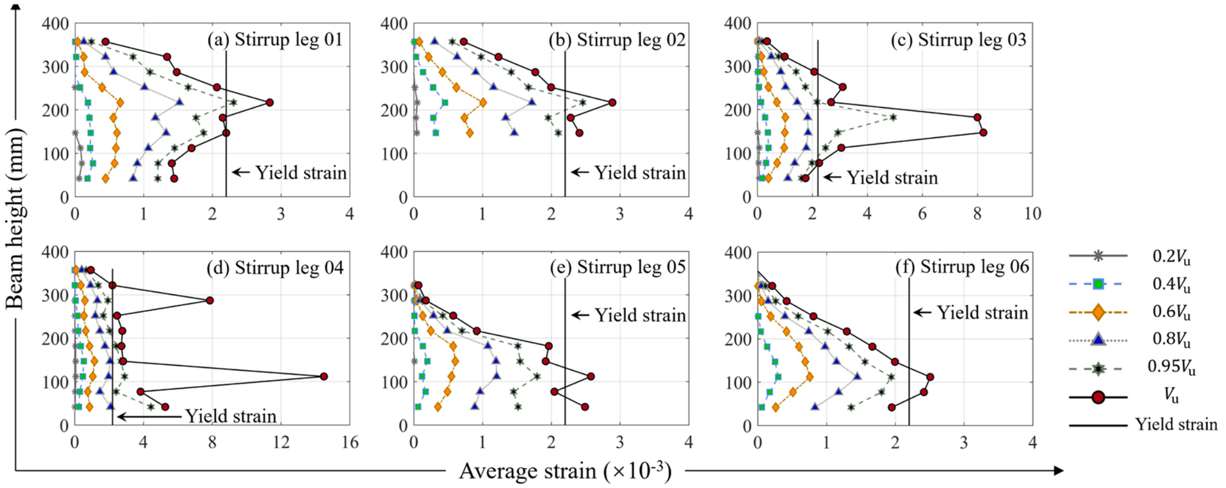

Fig. 15. Strain measurements along stirrups at selected loading levels in R/E-S.

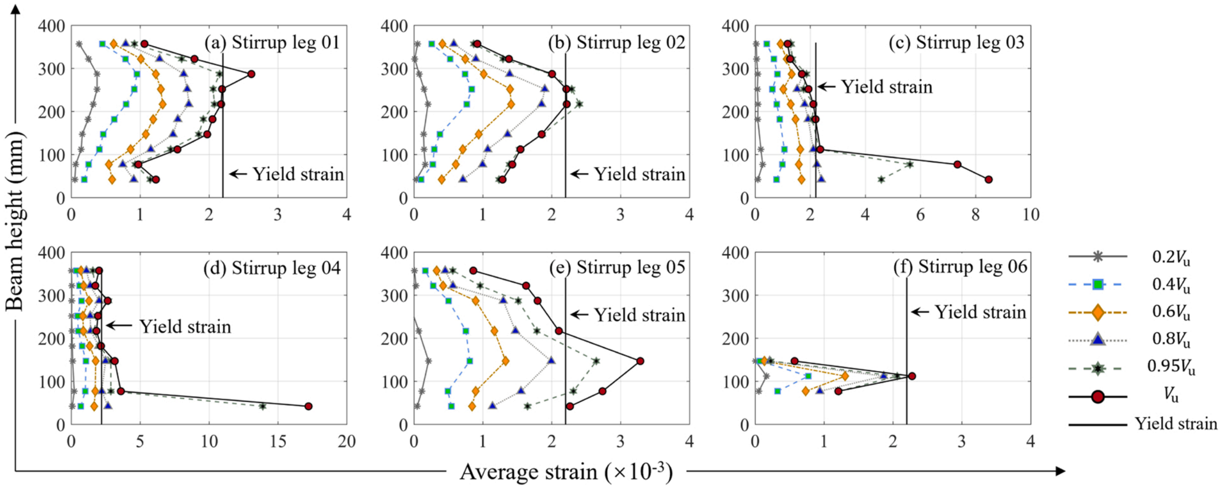

Fig. 16. Strain measurements along stirrups at selected loading levels in R/M-S.

Nevertheless, the rigid-body-rotation of shear crack could cause an underestimation of ω but overestimation of Δ. Such effect can be eliminated through establishment of a local coordinate system within the cracking area of interest, as illustrated in Fig. 18(b). That is, record the displacements of two additional surrounding calculation points C and D (denoted by C′ and D′ after the beam's deformation), and the rigid-body-rotating angle α can be determined by the average rotation of local coordinate system A-B-C and D-A-B, as expressed by Eq. (4). Then, the expression of shear crack kinematics can be modified as Eqs. (5) and (6). To simplify the calculation, the elastic deformation of the area A-B-C-D is neglected considering its negligible role in causing nodal displacements compared with cracking [28,48].

$$\omega = \frac{\overrightarrow{AB} \bullet \overrightarrow{A'B'}}{\left|\overrightarrow{AB}\right|} - \left|\overrightarrow{AB}\right| \tag{2}$$

$$\Delta = \left|\overrightarrow{A'B'}\right| \bullet \sin\left(\arccos\frac{\overrightarrow{AB} \bullet \overrightarrow{A'B'}}{\left|\overrightarrow{AB}\right|\left|\overrightarrow{A'B'}\right|}\right) \tag{3}$$

$$\alpha = \frac{1}{2}\left(\arccos\frac{\overrightarrow{BC} \bullet \overrightarrow{B'C'}}{\left|\overrightarrow{BC}\right|\left|\overrightarrow{B'C'}\right|} + \arccos\frac{\overrightarrow{AD} \bullet \overrightarrow{A'D'}}{\left|\overrightarrow{AD}\right|\left|\overrightarrow{A'D'}\right|}\right) \tag{4}$$

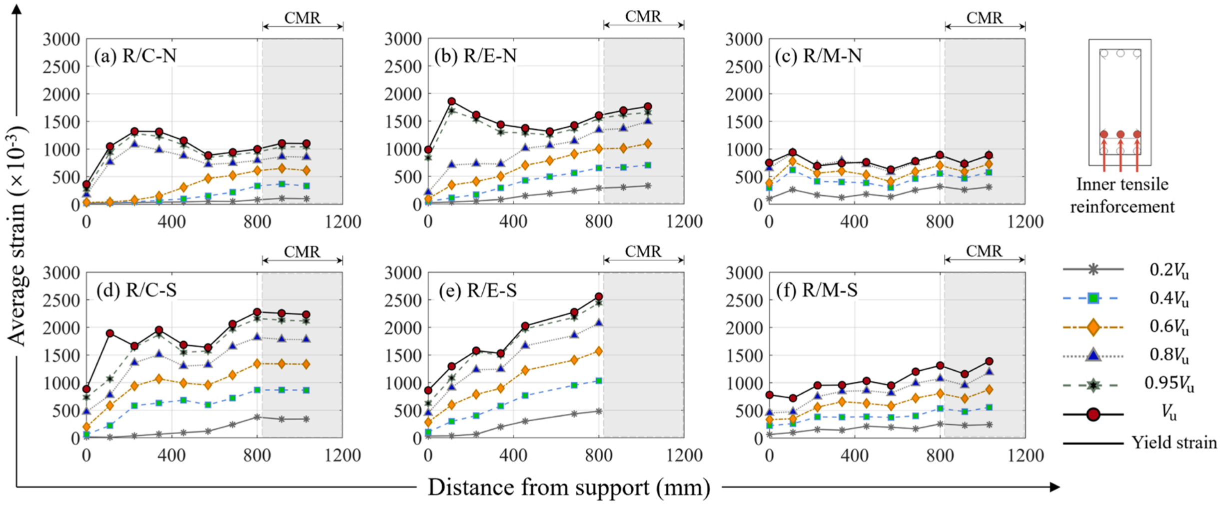

Fig. 17. Strain measurements along longitudinal tensile reinforcement of inner layer at selected loading levels ('CMR' represents constant moment region).

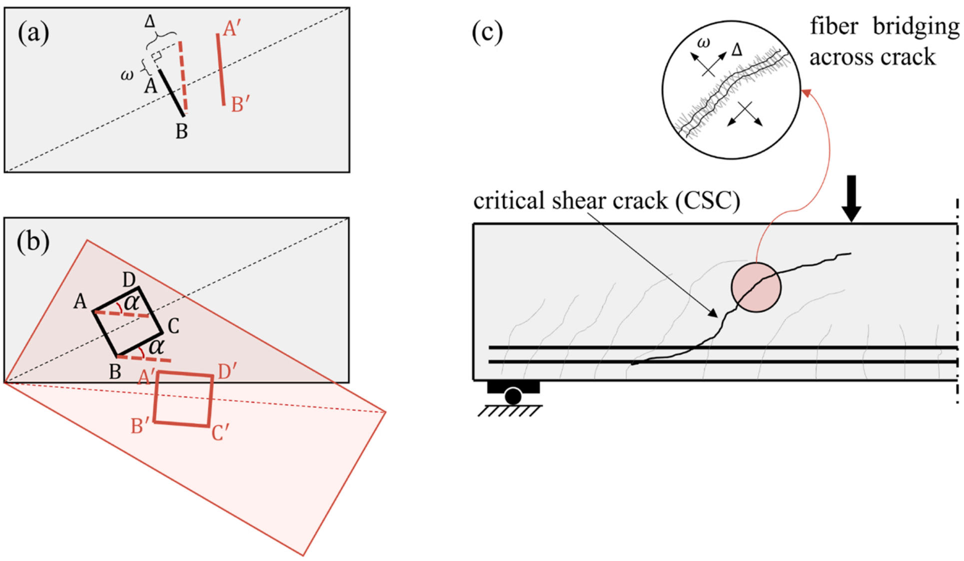

Fig. 18. Schematic illustration of shear crack kinematics quantification: (a) area without rigid-body-rotation; (b) area with rigid-body-rotation; (c) local view of fiber's bridging across the CSC (ω and Δ represent the shear crack opening and sliding displacements respectively; α represents the rigid-body-rotating angle).

$$\omega = \left|\overrightarrow{A'B'}\right| \cos\left(\arccos \frac{\overrightarrow{AB} \bullet \overrightarrow{A'B'}}{\left|\overrightarrow{AB}\right|\left|\overrightarrow{A'B'}\right|} - \alpha \right) - \left|\overrightarrow{AB}\right| \tag{5}$$

$$\Delta = \left|\overrightarrow{A'B'}\right| \sin\left(\arccos \frac{\overrightarrow{AB} \bullet \overrightarrow{A'B'}}{\left|\overrightarrow{AB}\right|\left|\overrightarrow{A'B'}\right|} - \alpha \right) \tag{6}$$

By selecting a set of gauging area (each gauging area contains four calculation points as illustrated in Fig. 18b) along the CSC (Fig. 19), the propagation and distribution of shear crack opening and sliding can be obtained. The shear crack opening and sliding displacements against the beam's deflection within the gauging area CR4, CR5 and CR6 are shown in Fig. 20 ('CR' represents the local gauging area along the CSC, and each gauging area contains four calculation points as illustrated in Fig. 18b), and the moments when the first and last stirrup legs yielded are both marked. The crack opening and sliding displacements along the full-length of CSC at the peak load in six beams are listed in Table 5.

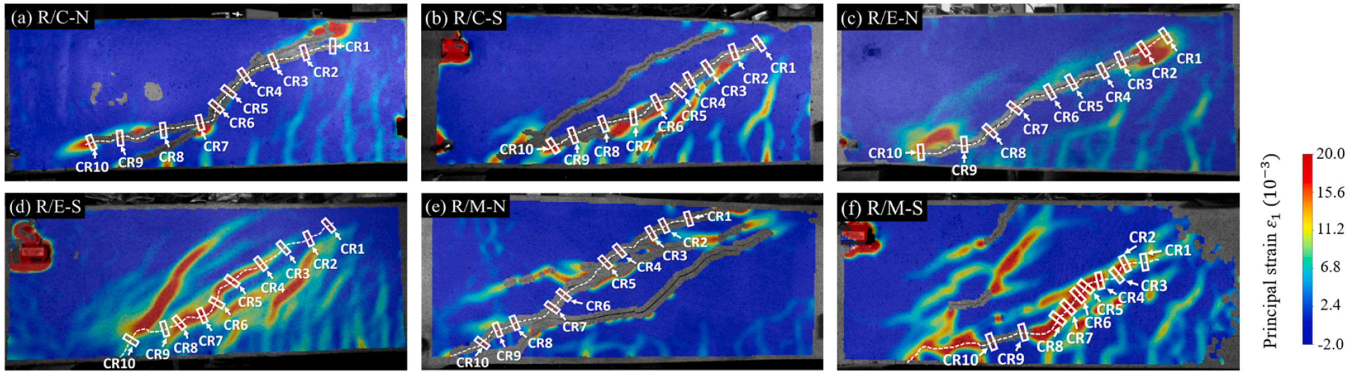

Fig. 19. Gauging area for quantifying the critical shear crack kinematics of the beam: (a) R/C-N; (b) R/C-S; (c) R/E-N; (d) R/E-S; (e) R/M-N; (f) R/M-S (the exhibited principal strain spectra corresponds to each beam's peak load; 'CR' represents the gauging area, and each gauging area contains four calculation points as illustrated in Fig. 18b).

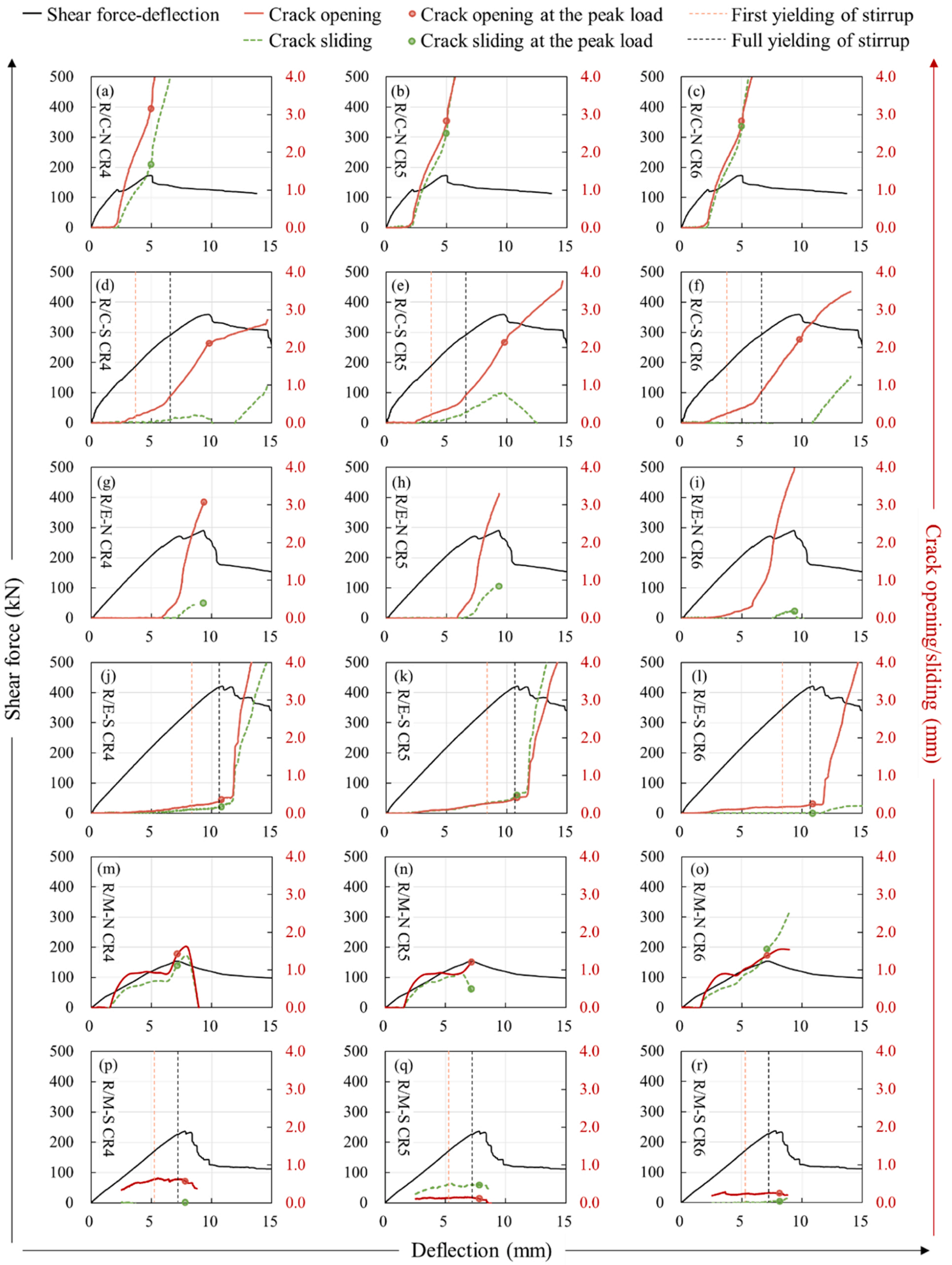

(caption on next page)

Fig. 20. Crack opening and sliding displacements against the deflection within the gauging area: (a) to (c) depict CR4, CR5 and CR6 in R/C-N, respectively; (d) to (f) depicts CR4, CR5 and CR6 in R/C-S, respectively; (g) to (i) depicts CR4, CR5 and CR6 in R/E-N, respectively; (j) to (l) depicts CR4, CR5 and CR6 in R/E-S, respectively; (m) to (o) depicts CR4, CR5 and CR6 in R/M-N, respectively; (p) to (r) depicts CR4, CR5 and CR6 in R/M-S, respectively (the crack displacement before 80 kN was missing due to the loss of DIC images).

In the concrete beam without stirrups R/C-N, several flexural cracks initiated from the bottom of the beam and propagated to CR6, where the shear crack opening was detected once the load reached around 100 kN. With load increasing, the vertical crack widened, and gradually rotated and stretched to CR5 (115 kN) and CR4 (120 kN) without obvious sliding. When the load reached 125 kN (the crack opening at CR6, CR5 and CR4 was 0.16 mm, 0.15 mm and 0.14 mm, respectively), crack sliding happened accompanied by a sudden drop of load, and a secondary splitting crack along the bottom tensile reinforcement appeared. With the stress redistribution, the load could increase again but the shear crack opening and sliding accelerated, and the beam lost its shear resistance finally due to the crushing of concrete underneath the loading point. When concrete beam is reinforced by stirrups (R/C-S), the crack propagation was rather controlled. Before the yielding of stirrups (188 kN), steady shear crack opening was observed without obvious sliding. After yielding, the crack sliding happened and was first detected at CR5. When the shear force increased to 289 kN, all six stirrup legs yielded, which resulted in an accelerated crack opening as shown in Fig. 20 (d) to (f).

In the ECC beam R/E-N without stirrup, a small drop of load could be found when the shear force was increased to 271 kN. After that, the increase of crack opening and sliding accelerated. At the peak load, the maximum crack opening and sliding along the CSC was detected to be 3.90 mm (CR6) and 2.78 mm (CR7), respectively, which were larger than those in the reference concrete beam. In the ECC beam R/E-S with stirrups, a steadier shear crack propagation was found compared with other three beams. When the shear load was increased to 344 kN, yielding of rebar took place, firstly in the stirrup leg 04 (Fig. 13), at a much higher load (83% more) than that in the reference concrete beam (first yielding of stirrup happened at 188 kN). The initial yielding of stirrup did not expedite the shear crack sliding and opening in ECC, which happened until all six stirrup legs yielded under a shear force of 416 kN. With a tiny increase of load (to 421 kN), the shear strength of the beam was reached, and the maximum shear crack opening was below 0.51 mm. After a slight drop of load (to 409 kN), the shear force increased again to 419 kN (Fig. 20 j, k and l). Then, a sudden increase in the CSC opening and sliding happened leading to the ultimate failure of beam.

In the concrete and ECC beams, the shear crack opening usually took place earlier than the sliding, revealing that the shear crack originated from the tensile fracture of concrete and ECC matrix. However, in the mortar beams, the crack could slide immediately upon its formation due to the absence of aggregates or fibers. In R/M-S, it was interesting to find a multiple cracking behavior (Fig. 19f) similar as R/E-S (Fig. 19d), and the maximum shear crack opening was only 0.94 mm when the beam's shear strength was reached.

4.2. Shear crack kinematics along the beam height

By selecting and analysing a set of points along the CSC, the crack kinematics along the beam height under selected loading levels can be obtained, as shown in Fig. 21 and Fig. 22. In the concrete and ECC beams, the CSC had largest width near the beam's mid-height, which appeared as a special fusiform crack. The crack sliding showed a similar distribution pattern as opening, and the ends of CSC (near the loading and supporting points) exhibited almost no sliding. Comparing the crack opening distribution at two different loading levels $0.95V_u$ and V_u, it can be found that a 5% increase of load could cause over 20% increase in the crack opening displacement, revealing severe shear crack width growth near the peak load and the brittle nature of shear failure.

Most shear strength models established for R/ECC beams consider the fiber bridging's contribution along the CSC [16,29,34–37]. Through the equilibrium of free body in Fig. 23, the fiber bridging's contribution can be counted as $\mu_t f_{tu} bz\cot\varphi$, where μ_t is the tensile strength reduction factor of ECC. In two R/ECC structural design specifications T/CECS 1212-2022 [36] and JSCE 08 [37], μ_t is taken as 0.5 and 1.0 separately, revealing that the residual tensile stress is 50% or 100% the tensile strength of ECC. However, such assumption may be not suitable always. In the ECC beam R/E-N with no stirrups, the CSC had an opening over 2.0 mm at its peak load (Fig. 21b). Such crack width in typical PVA-ECC implies that the bridging stress is almost lost and μ_t approached zero [1,38,49,50]. Nevertheless, the ECC beam R/E-N still exhibited 68% higher shear strength than the reference concrete beam R/C-N. Therefore, not the fiber's bridging across the shear cracks, but some other shear-resisting mechanisms in the R/ECC beam should be responsible for its high shear carrying capacity. One potential mechanism is a high shear-resisting contribution from ECC in shear-compression zone, which is denoted as V_a (Fig. 23). It has been proved that ECC has high shear strength and deformational ability under combined compression and shear [51,52], and the shear strength of R/C beam (with no stirrup, shear span-to-effective depth ratio is 2.5) can be enhanced by about 93% through locally substituting concrete with ECC in shear-compression zone [53]. Additionally, the dowel action of bottom tensile reinforcement also plays an important role in resisting shear, and such contribution depends primarily on the tensile resistance of material along the splitting cracks [54–56]. However, the investigation of dowel action in R/ECC is still limited, and more evidence should be provided through future work.

4.3. Shear strength components against maximum shear crack width

The shear carrying capacity (V_u) can be divided into two parts: contribution of matrix (V_c) and stirrups (V_s). The V_s can be accurately acquired by extracting the stirrup strain exactly at the CSC (Eq. 1), and then V_c can be obtained by deducting V_s from V_u. Note that the net cross-sectional area of stirrup leg was used when calculating V_s, which should be 95.1 mm^2 by taking the cavity out. The variation of V_c and V_s against the maximum shear crack width in three beams with stirrups is shown in Fig. 24. Before cracking, the

Table 5

The CSC opening and sliding displacements at the peak load in all beams.

Gauging area	R/C-N		R/C-S		R/E-N		R/E-S		R/M-N		R/M-S	
	ω (mm)	Δ (mm)	ω (mm)	Δ (mm)	ω (mm)	Δ (mm)	ω (mm)	Δ (mm)	ω (mm)	Δ (mm)	ω (mm)	Δ (mm)
CR1	0.89	0.00	0.85	0.00	0.42	0.04	0.01	0.00	1.10	0.19	0.32	0.00
CR2	1.47	0.00	– (0.96)	– (0.00)	0.47	0.14	0.01	0.00	1.18	0.42	0.44	0.39
CR3	– (2.51)	– (0.35)	1.68	0.17	2.08	0.00	0.20	0.13	1.05	0.45	0.59	0.14
CR4	**3.07**	1.63	2.11	0.11	3.02	0.35	0.37	0.19	1.42	1.12	0.58	0.00
CR5	2.68	2.38	2.13	0.81	3.24	0.81	0.43	0.47	1.20	0.45	0.11	0.47
CR6	2.62	2.46	**2.19**	0.00	**3.90**	0.17	0.24	0.01	1.39	1.55	0.25	0.05
CR7	3.00	0.00	– (1.85)	– (0.00)	2.78	3.24	**0.51**	0.00	1.12	1.69	0.11	0.19
CR8	2.23	0.00	1.66	0.00	3.38	1.98	0.39	0.13	**2.04**	0.00	0.17	0.29
CR9	1.25	0.00	– (1.34)	– (0.00)	2.75	0.00	0.20	0.00	1.44	0.00	**0.94**	0.00
CR10	0.74	0.00	– (1.18)	– (0.00)	0.63	0.00	0.18	0.24	0.88	0.52	0.88	0.00

Notes: ω and Δ represent the shear crack opening and sliding displacements respectively; 'CR' represents the gauging area, and each gauging area contains four calculation points; the symbol '–' means data lost within certain gauging area due to image correlation failure under large deformation, and the data in brackets were the last valid detected crack displacements before the image correlation failure.

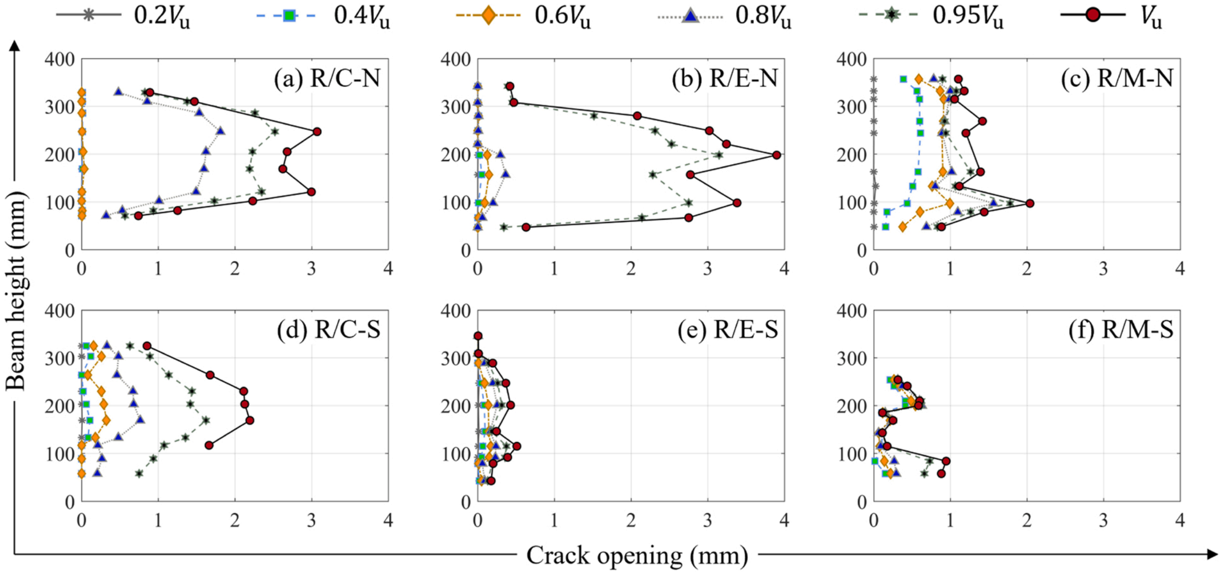

Fig. 21. Critical shear crack opening displacements along the beam height under selected loading levels: (a) R/C-N; (b) R/E-N; (c) R/M-N; (d) R/C-S; (e) R/E-S; (f) R/M-S.

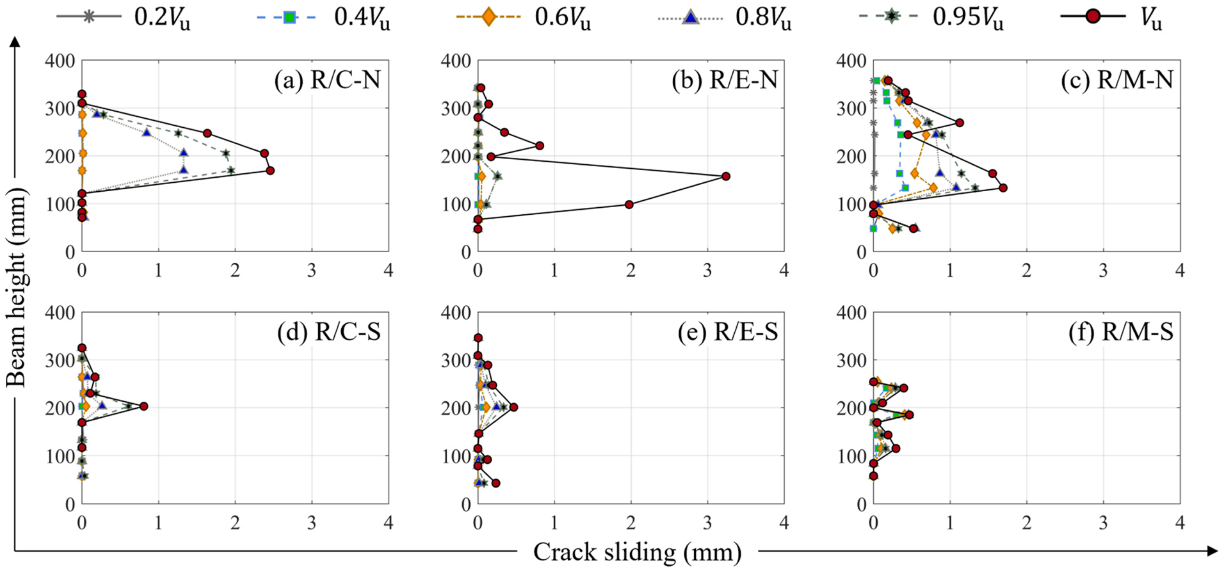

Fig. 22. Critical shear crack sliding displacements along the beam height under selected loading levels: (a) R/C-N; (b) R/E-N; (c) R/M-N; (d) R/C-S; (e) R/E-S; (f) R/M-S.

shear load was almost solely undertaken by V_c in all beams. When the shear crack appeared, a decrease of V_c happened in R/C-S and R/M-S, upon which the V_s was activated. Differently, the V_c in R/E-S could steadily increase until approaching the beam's ultimate strength. Furthermore, the V_c, V_s and V_u did not reach their peak values simultaneously in all beams. More specifically, the V_c reached its peak a little bit earlier than V_u, and V_s could even increase after reaching V_u due to the further yielding or hardening of stirrups. Finally, the beam R/E-S exhibited a V_c 104% higher than that of R/C-S, but the V_s was 24% lower due to the incomplete yielding of stirrups along the CSC in ECC (as shown in Fig. 15). In R/M-S, it is interesting to find that V_c was almost lost after the shear cracking, revealing the important role of aggregate interlock or fiber bridging in transferring shear across cracks.

Compared with the beams with no stirrups, the V_c in R/C, R/ECC and R/M beams with a stirrup ratio of 0.38% were reduced by about 34%, 20% and 93% respectively, revealing a negative effect between V_c and V_s in all types of beams.

In previous research [28–31], the V_s was always evaluated by using the mid-height strain of stirrups instead of the actual strain along the CSC. To verify the possible deviation, a comparison is made between two strain-measuring schemes in Fig. 25. Based on the

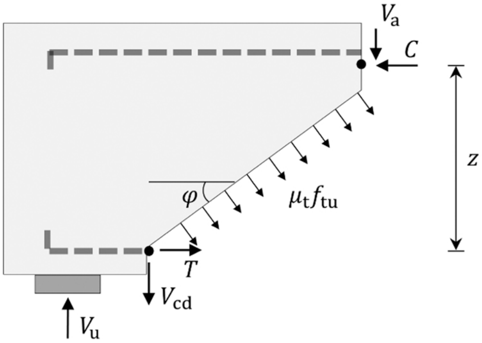

Fig. 23. Equilibrium of free body considering the fiber's contribution in resisting the shear force.

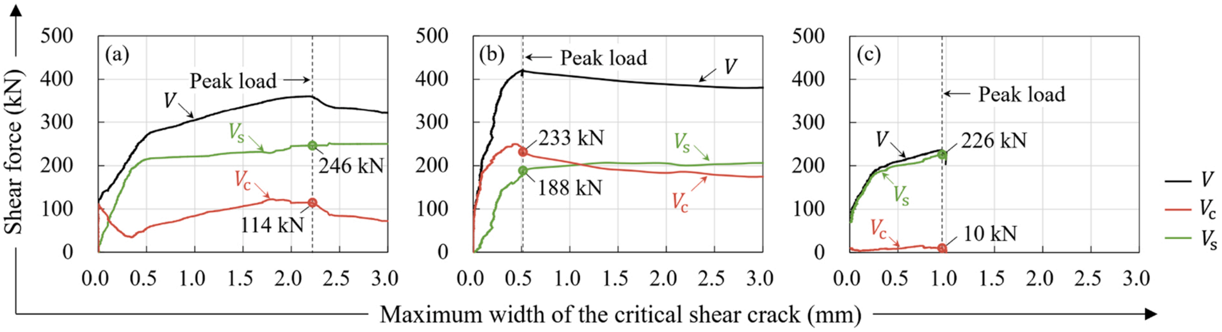

Fig. 24. The variation of V_c and V_s against the maximum width of the CSC: (a) R/C-S; (b) R/E-S; (c) R/M-S.

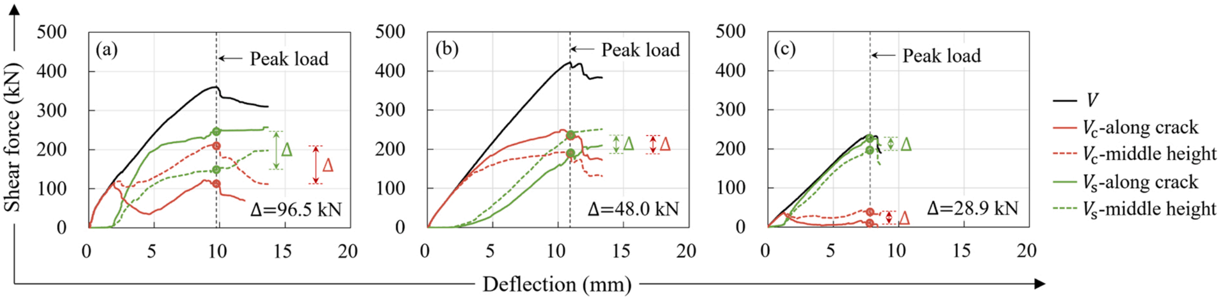

Fig. 25. Comparison of V_c and V_s determined by different strain-measuring schemes: (a) R/C-S; (b) R/E-S; (c) R/M-S (V is the total shear force, V_c-along crack and V_s-along crack are the calculated V_c and V_s using the stirrups' strain along the CSC, V_c-middle height and V_s-middle height are the calculated V_c and V_s using the stirrups' strain at the beam's middle height).

former approach, the V_s is underestimated by 39% in R/C-S but overestimated by 26% in R/E-S at the peak load, and consequently a contrary tendency is found in V_c (overestimated by 85% in R/C-S and underestimated by 21% in R/E-S). The variation of shear strength components against the deflection is also significantly altered, e.g., the long drop in V_c after shear cracking does not appear any more in R/C-S (Fig. 25a). Considering that one stirrup leg could be crossed by more than one shear cracks, the stirrup strain at the beam's mid-height might be either higher or lower than that along the CSC, as depicted in Fig. 14 to Fig. 16. Therefore, it is hard to conclude using the mid-height strain should cause over- or under-estimation in V_c and V_s. However, it has been proved that the V_c and V_s can be accurately evaluated only when the full-length strain distribution along the stirrup legs are obtained.

4.4. Phenomenological model of shear crack kinematics

To explore the shear crack kinematics, the nominal shear stress against the crack opening and sliding of selected gauging points (CR4 to CR7) along the CSC in concrete and ECC beams are shown in Fig. 26. The initial shear cracking stress in R/C and R/ECC was almost the same (1.5 MPa) as concrete and ECC had similar compressive (and first cracking) strength. Under a same load level of 2.6 MPa (the ultimate shear strength of R/C-N), the maximum shear cracking opening displacements in R/E-N and R/E-S were 1/26

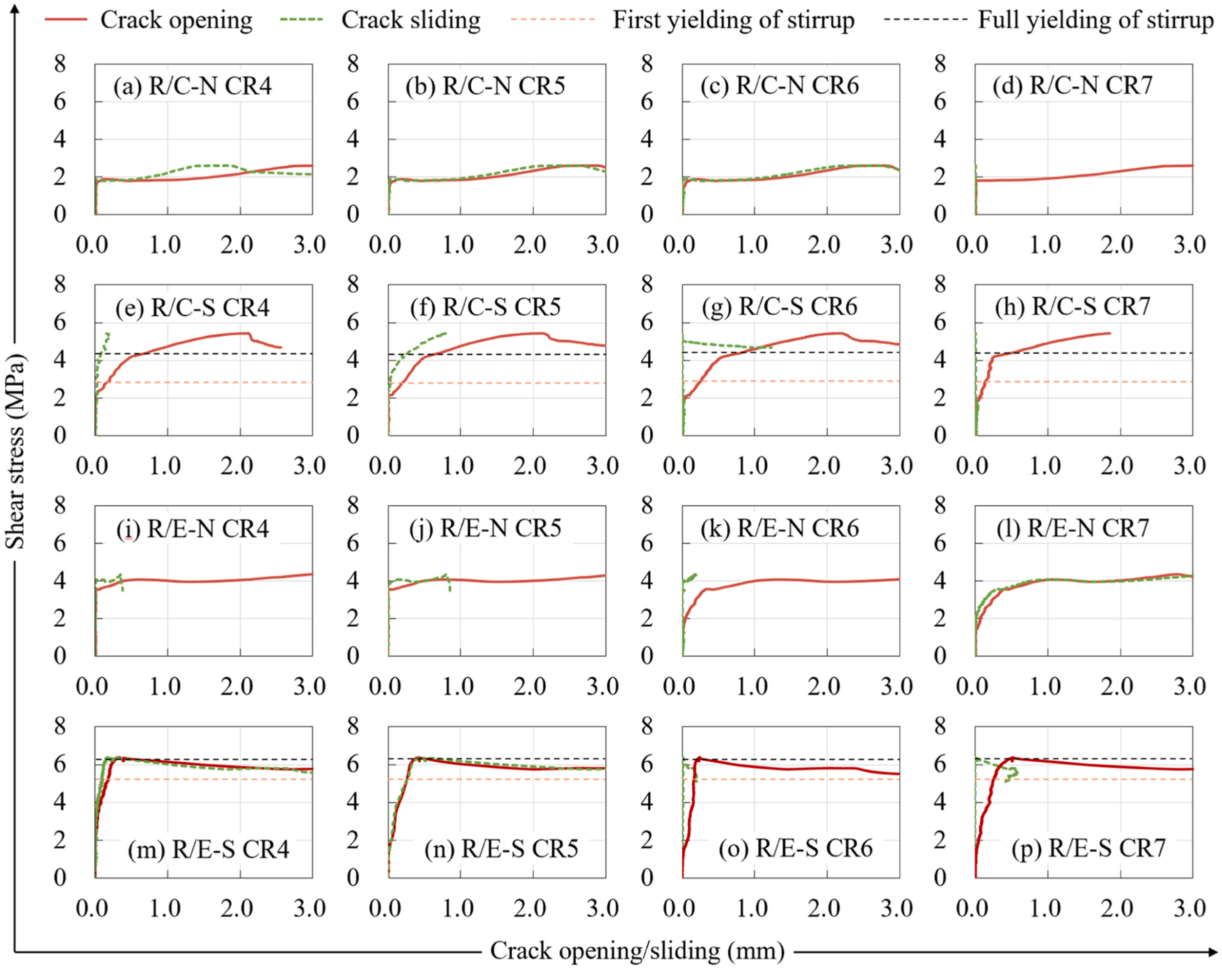

Fig. 26. Shear stress against the crack opening and sliding displacements of selected gauging points along the CSC: (a) to (d) depicts CR4, CR5 and CR6 in R/C-N, respectively; (e) to (h) depicts CR4, CR5 and CR6 in R/C-S, respectively; (i) to (l) depicts CR4, CR5 and CR6 in R/E-N, respectively; (m) to (p) depicts CR4, CR5 and CR6 in R/E-S, respectively.

and 1/3 (0.12 mm and 0.07 mm) of those in R/C-N and R/C-S (3.07 mm and 0.20 mm). The first yielding of stirrup was delayed in R/E-S, with the corresponding shear stress 83% higher than that in R/C-S, revealing a more synergistic deformation between ECC and rebar.

For a better understanding of the shear-resisting and failure mechanism in R/C and R/ECC beams, phenomenological models of shear crack kinematics in different types of beams are proposed based on the test results, which are separately illustrated in Fig. 27 and descripted as follows:

- **R/C beam without stirrups** (Fig. 27a): (1) the inclined shear crack firstly initiates from the rotation of vertical flexure crack; (2) the shear crack suddenly widens with maintained load (or even slightly load drop), during which sliding happens and the aggregate interlock is activated; (3) the load continues to increase and the shear crack propagates to both loading and supporting points along with the increase of crack opening and sliding, when a secondary splitting crack forms along the longitudinal reinforcement due to the rebar's dowel action; (4) the beam fails when the concrete in shear-compression zone crushes.
- **R/C beam with stirrups** (Fig. 27b): (1) the inclined shear crack firstly initiates from the rotation of vertical flexure crack, and then stirrups are activated once crossed by the shear crack; (2) as load continues to increase, sliding happens, the aggregate interlock takes part in resisting shear, and stirrups start yielding; (3) all stirrups yield, leading to an accelerated shear crack opening and sliding; (4) the beam fails when the concrete in shear-compression zone crushes.
- **R/ECC beam without stirrups** (Fig. 27c): (1) similar to the R/C beams, the inclined shear crack firstly initiates from the rotation of vertical flexure crack; (2) the crack sliding happens; (3) the crack opening and sliding accelerates as fiber bridging effect decrease, and the secondary splitting crack can form along the longitudinal reinforcement and dowel action is activated; (4) the beam fails when the ECC in shear-compression zone crushes.

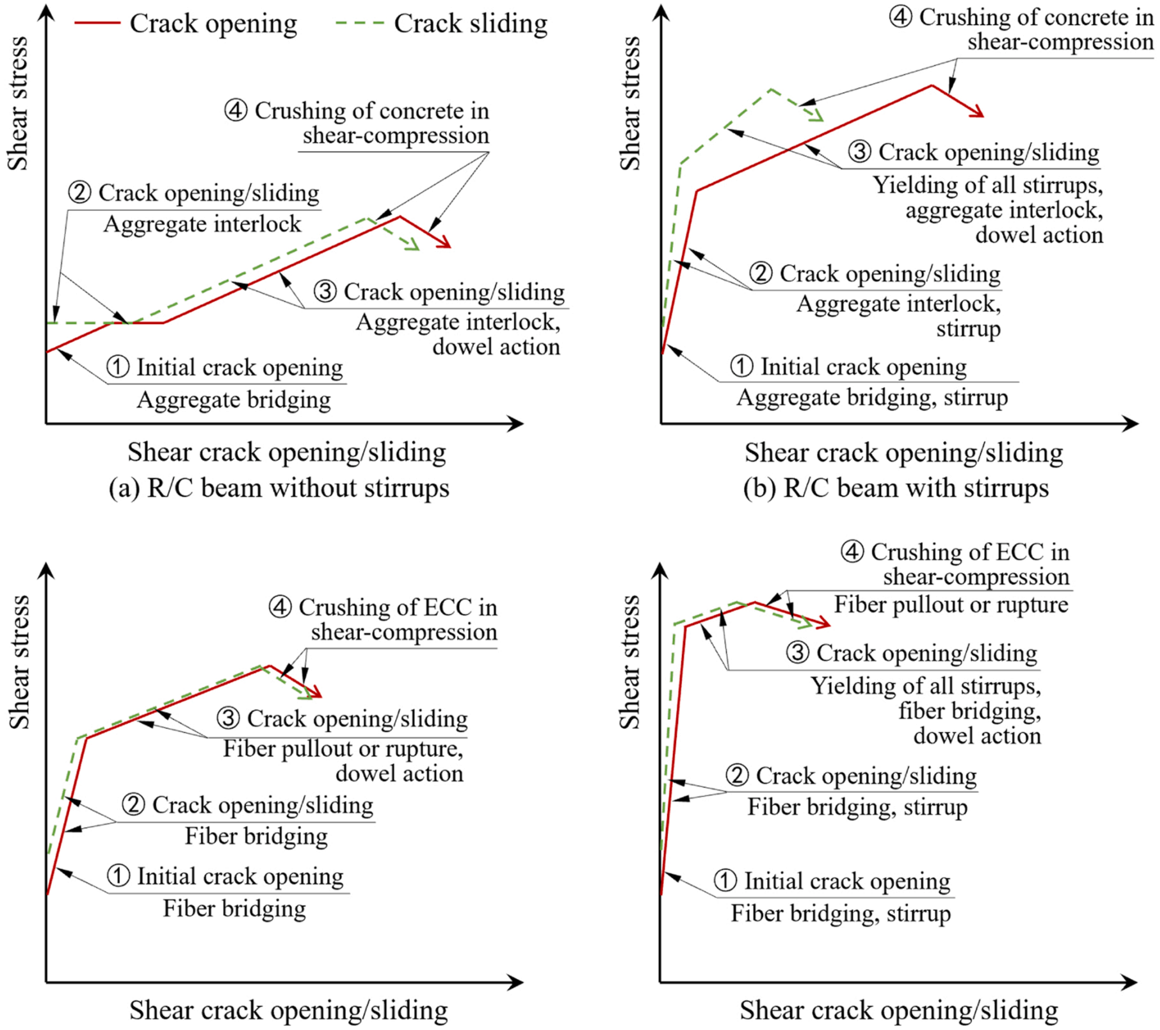

(a) R/C beam without stirrups

(b) R/C beam with stirrups

(c) R/ECC beam without stirrups

(d) R/ECC beam with stirrups

Fig. 27. Phenomenological description of shear crack kinematics in: (a) R/C beam without stirrup; (c) R/C beam with stirrups; (c) R/ECC beam without stirrup; (d) R/ECC beam with stirrups.

- **R/ECC beam with stirrups** (Fig. 27d): (1) the inclined shear crack firstly initiates from the rotation of vertical flexure crack, and stirrups crossed by the shear crack are activated; (2) later sliding happens at increased load, and stirrups start yielding; (3) all stirrups yield followed by an accelerated shear crack opening and sliding; (4) the beam reaches its shear strength due to the crushing of ECC in shear-compression zone, after which the shear crack opening and sliding increase rapidly and the bridging ability of fiber is finally lost due to excessive crack opening.

Note that the aforementioned phenomenological models are proposed based on the test results of beams with specific geometric size and boundary condition in this research, which should be examined by more shear tests.

5. Conclusions

In this research, the shear behavior of R/C and R/ECC beams was investigated. An algorithm for quantifying the shear crack kinematics (opening and sliding) is developed based on the full-field displacement spectrum detected by the DIC system. By a distributed strain-measuring scheme the shear-resisting components V_c and V_s could be accurately evaluated. The following conclusions are drawn:

- The V_c and V_s can be accurately quantified only when the full-length strain distribution along the stirrup legs are obtained. Evaluating V_s by using the stirrup strain at half-height can cause obvious deviation. Besides, assuming that all stirrups crossed by the CSC yield is likely to cause overestimation of V_s.

- The shear load was almost all taken by V_c before the formation of shear cracks. After shear cracking, the V_c dropped in the R/C beam but stably increased in the R/ECC ones. At the peak load, the V_c in R/ECC was 104% higher than that in R/C, but the V_s was 24% lower due to the incomplete yielding of stirrups.
- In the R/C and R/ECC beams, the shear crack opening usually took place earlier than the sliding, revealing that the shear crack originated from the tensile fracture of matrix, this is in line with conclusions from [28,57]. Spindle-shaped critical shear cracks were observed, which had the largest width (crack opening) near the beams' mid-height. The crack sliding displacement also varied along the beams' height, and two ends of CSC (near the loading and supporting points) exhibited almost no sliding but only opening displacement.
- When the ECC beam with no stirrups (R/E-N) reached its peak load, an opening of its CSC was more than 2.0 mm. It signified that the fiber's bridging effect across the shear crack almost exhausted, which was inconsistent with the assumptions of some existing shear strength predicting models for R/ECC (regarding ECC's tensile strength as the residual tensile stress of the CSC). Nevertheless, the ECC beam R/E-N still exhibited 68% higher shear strength than the reference concrete beam R/C-N, revealing that some other shear-resisting mechanisms were more effectively released in ECC such as higher shear force taken by the shear-compression zone and dowel action of the longitudinal reinforcement.

Note that above conclusions are limited to the tested specimens in this research, and more tests are expected in the future to further investigate the influence of shear span-to-effective depth ratio, transverse and longitudinal reinforcement ratio on the shear crack kinematics of reinforced ECC.

CRediT authorship contribution statement

Mladena Luković: Writing – review & editing, Supervision. **Jinlong Pan:** Writing – review & editing, Supervision, Investigation, Funding acquisition, Conceptualization. **Yitao Huang:** Software, Methodology, Investigation. **Haowen Xu:** Visualization, Software, Investigation, Data curation. **Yusen Zhu:** Methodology, Investigation. **Dawei Gu:** Writing – review & editing, Writing – original draft, Validation, Software, Methodology, Investigation, Funding acquisition, Data curation, Conceptualization.

Declaration of Competing Interest

The authors declared that they have no conflicts of interest to this work. We declare that we do not have any commercial or associative interest that represents a conflict of interest in connection with the work submitted.

Data availability

Data will be made available on request.

Acknowledgement

The work is financially supported by the National Natural Science Foundation of China (No. 52278155) and Natural Science Foundation of Jiangsu Province (BK20230860).

References

[1] E.H. Yang, S. Wang, Y. Yang, V.C. Li, Fiber-bridging constitutive law of engineered cementitious composites, J. Adv. Concr. Technol. 6 (2008) 181–193, https://doi.org/10.3151/jact.6.181.
[2] Z. Li, J. Zhou, C.K.Y. Leung, Fiber orientation distribution in strain hardening cementitious composites (SHCC): experimental investigation and consideration of processing effect, Cem. Concr. Res. 170 (2023) 107190, https://doi.org/10.1016/j.cemconres.2023.107190.
[3] V.C. Li, C.K.Y. Leung, Steady-state and multiple cracking of short random fiber composites, J. Eng. Mech. 118 (1992) 2246–2264, https://doi.org/10.1061/(asce)0733-9399(1992)118:11(2246).
[4] E.H. Yang, Y. Yang, V.C. Li, Use of high volumes of fly ash to improve ECC mechanical properties and material greenness, ACI Mater. J. 104 (2007) 620–628, https://doi.org/10.14359/18966.
[5] Z. Zhang, A. Yuvaraj, J. Di, S. Qian, Matrix design of light weight, high strength, high ductility ECC, Constr. Build. Mater. 210 (2019) 188–197, https://doi.org/10.1016/j.conbuildmat.2019.03.159.
[6] J.X. Zhu, K.F. Weng, B.T. Huang, L.Y. Xu, J.G. Dai, Ultra-high-strength engineered cementitious composites (UHS-ECC) panel reinforced with FRP bar/grid: development and flexural performance, Eng. Struct. 302 (2024) 117193, https://doi.org/10.1016/j.engstruct.2023.117193.
[7] J.C. Lao, R.Y. Ma, L.Y. Xu, Y. Li, Y.N. Shen, J. Yao, Y.S. Wang, T.Y. Xie, B.T. Huang, Fly ash-dominated High-Strength Engineered/Strain-Hardening Geopolymer Composites (HS-EGC/SHGC): influence of alkalinity and environmental assessment, J. Clean. Prod. 447 (2024) 141182, https://doi.org/10.1016/j.jclepro.2024.141182.
[8] F. Gong, X. Sun, Y. Takahashi, K. Maekawa, W. Jin, Computational modeling of combined frost damage and alkali–silica reaction on the durability and fatigue life of RC bridge decks, J. Intell. Constr. 1 (2023) 9180001, https://doi.org/10.26599/jic.2023.9180001.
[9] Q.H. Li, A.M. Luo, B.T. Huang, G.Z. Wang, S.L. Xu, Bond behavior between steel bar and strain-hardening fiber-reinforced cementitious composites under fatigue loading, Eng. Struct. 314 (2024) 118354, https://doi.org/10.1016/j.engstruct.2024.118354.
[10] Z. Cheng, J. Zhang, J. Tang, X. Ren, H. Li, Peridynamic model of ECC-concrete composite beam under impact loading, Eng. Fract. Mech. 295 (2024) 109791, https://doi.org/10.1016/j.engfracmech.2023.109791.
[11] Z.F. Akbulut, D. Yavuz, T.A. Tawfik, P. Smarzewski, S. Guler, Enhancing Concrete Performance through Sustainable Utilization of Class-C and Class-F Fly Ash: a comprehensive review, Sustainability 16 (2024) 4905, https://doi.org/10.3390/su16124905.

[12] S. Guler, Z.F. Akbulut, The coupling effect of silica fume and basalt fibers on workability and residual strength capacities of traditional concrete before and after freeze–thaw cycles, Arch. Civ. Mech. Eng. 23 (2023) 1–15, https://doi.org/10.1007/s43452-023-00719-2.

[13] V.C. Li, D.K. Mishra, A.E. Naaman, J.K. Wight, J.M. LaFave, H.C. Wu, Y. Inada, On the shear behavior of engineered cementitious composites, Adv. Cem. Based Mater. 1 (1994) 142–149, https://doi.org/10.1016/1065-7355(94)90045-0.

[14] G.P.A.G. van Zijl, Improved mechanical performance: shear behaviour of strain-hardening cement-based composites (SHCC), Cem. Concr. Res. 37 (2007) 1241–1247, https://doi.org/10.1016/j.cemconres.2007.04.009.

[15] T. Kanda, S. Nagai, M. Maruta, Y. Yamamoto, New high-rise R/C structure using ECC coupling beams, 2nd International RILEM Conference on Strain Hardening Cementitious Composites, Rio de Janeiro, Brazil, 2011, pp. 289–296.

[16] K. Shimizu, T. Kanakubo, T. Kanda, N. Saotoru, Shear behavior of steel reinforced PVA-ECC beams, 13th World Conference on Earthquake Engineering, Vancouver, Canada, 2004. https://doi.org/10.5459/bnzsee.38.1.41-49.

[17] T. Kanakubo, K. Shimizu, T. Kanda, S. Nagai, Evaluation of bending and shear capacities of HPFRCC members toward the structural application, Hokkaido University COE Workshop on High Performance Fiber Reinforced Composites for Sustainable Infrastructure System – Material Modeling, Structural Design and Application, Sapporo, Japan, 2007, pp. 1–10.

[18] X. Yang, L. Xu, J. Pan, Mechanical behavior of full-scale composite steel plate shear wall restrained by ECC panels, J. Build. Eng. 44 (2021) 102864, https://doi.org/10.1016/j.jobe.2021.102864.

[19] B. Ye, H. Wang, Y. Ma, P. Pan, Seismic performance of flexure-dominated reinforced-engineered cementitious composites coupled shear wall, Eng. Struct. 272 (2022) 114992, https://doi.org/10.1016/j.engstruct.2022.114992.

[20] Y. Zhang, M. Deng, Z. Dong, Seismic response and shear mechanism of engineered cementitious composite (ECC) short columns, Eng. Struct. 192 (2019) 296–304, https://doi.org/10.1016/j.engstruct.2019.05.019.

[21] C. Wu, Y. Su, C. Jin, Z. Pan, S. Meng, Seismic performance analysis of RC frames with ECC short columns based on the IDA method, Buildings 12 (2022) 1834, https://doi.org/10.3390/buildings12111834.

[22] R. Zhang, K. Matsumoto, T. Hirata, Y. Ishizeki, J. Niwa, Application of PP-ECC in beam-column joint connections of rigid-framed railway bridges to reduce transverse reinforcements, Eng. Struct. 86 (2015) 146–156, https://doi.org/10.1016/j.engstruct.2015.01.005.

[23] C.C. Hung, H.J. Hsiao, Y. Shao, C.H. Yen, A comparative study on the seismic performance of RC beam-column joints retrofitted by ECC, FRP, and concrete jacketing methods, J. Build. Eng. 64 (2023) 105691, https://doi.org/10.1016/j.jobe.2022.105691.

[24] F.A. Khan, S.W. Khan, W. Khan, Seismic performance of RC-ECC composite frame by eliminating shear reinforcement in beam-column joint: shake table tests, Adv. Struct. Eng. 25 (14) (2022) 2966–2980, https://doi.org/10.1177/13694332221113044.

[25] A. Hassan, A.T. Baraghith, A.M. Atta, T.F. El-Shafiey, Retrofitting of shear-damaged RC T-beams using U-shaped SHCC jacket, Eng. Struct. 245 (2021) 112892, https://doi.org/10.1016/j.engstruct.2021.112892.

[26] B. Hu, X. Wang, Y. Zhou, X. Huang, Z. Zhu, Seismic performance of shear-critical RC columns strengthened by multiple composites considering shifted failure zone, Case Stud. Constr. Mater. 20 (2024) e02971, https://doi.org/10.1016/j.cscm.2024.e02971.

[27] D. Zhao, K. Li, J. Fan, Y. Wang, J. Zhu, Shear behavior of RC beams strengthened with high-strength steel strand mesh reinforced ECC: shear capacity, cracking and deformation, Eng. Struct. 298 (2024) 117081, https://doi.org/10.1016/j.engstruct.2023.117081.

[28] I. Paegle, G. Fischer, Phenomenological interpretation of the shear behavior of reinforced engineered cementitious composite beams, Cem. Concr. Compos. 73 (2016) 213–225, https://doi.org/10.1016/j.cemconcomp.2016.07.018.

[29] S. Xu, L. Hou, X. Zhang, Flexural and shear behaviors of reinforced ultrahigh toughness cementitious composite beams without web reinforcement under concentrated load, Eng. Struct. 39 (2012) 176–186, https://doi.org/10.1016/j.engstruct.2012.01.011.

[30] D. Gu, J. Pan, M. Luković, J. He, Experimental and analytical study on shear behavior of strain-hardening cementitious composite beams reinforced with fiber-reinforced polymer bars, Struct. Concr. 23 (2022) 1080–1099, https://doi.org/10.1002/suco.202100544.

[31] L. Hou, S. Xu, X. Zhang, D. Chen, Shear behaviors of reinforced ultrahigh toughness cementitious composite slender beams with stirrups, J. Mater. Civ. Eng. 26 (2014) 466–475, https://doi.org/10.1061/(asce)mt.1943-5533.0000833.

[32] J.J. Poldon, N.A. Hoult, E.C. Bentz, Understanding reinforcement behavior using distributed measurements of shear tests, ACI Struct. J. 118 (2021) 255–266. https://doi.org/10.14359/51730537.

[33] Y. Wu, B. Hu, Shear strength components in reinforced concrete members, J. Struct. Eng. 143 (2017) 1–16, https://doi.org/10.1061/(asce)st.1943-541x.0001832.

[34] D. Gu, J. Pan, S. Mustafa, Y. Huang, M. Luković, Shear transfer mechanism in reinforced engineered cementitious composite (ECC) beams: quantification of Vs and Vc, Eng. Struct. 261 (2022) 114282, https://doi.org/10.1016/j.engstruct.2022.114282.

[35] S. Xu, L. Hou, X. Zhang, Shear behavior of reinforced ultrahigh toughness cementitious composite beams without transverse reinforcement, J. Mater. Civ. Eng. 24 (2012) 1283–1294, https://doi.org/10.1061/(asce)mt.1943-5533.0000505.

[36] China Association for Engineering Construction Standardization (CECS), Technical specification for strain-hardening cementitious composites structures, China Planning Press, Beijing, 2022.

[37] Japan Society of Civil Engineers (JSCE), Recommendations for design and construction of high performance fiber reinforced cement composites with multiple fine cracks (HPFRCC), Tokyo, 2008..

[38] C. Wu, C.K.Y. Leung, V.C. Li, Derivation of crack bridging stresses in engineered cementitious composites under combined opening and shear displacements, Cem. Concr. Res. 107 (2018) 253–263, https://doi.org/10.1016/j.cemconres.2018.02.027.

[39] T. Kanakubo, K. Shimizu, S. Nagai, T. Kanda, Shear transmission on crack surface of ECC, 7th International Conference on Fracture Mechanics for Concrete and Concrete Structures (FraMCos-7). Jeju, Korea, 2010, pp.1623–1630.

[40] Q. Liao, J. Yu, T. Shi, Y. Su, Mechanical behaviors and failure criteria of seawater sea-sand engineered cementitious composites under combined tension and shear, J. Build. Eng. 54 (2022) 104552, https://doi.org/10.1016/j.jobe.2022.104552.

[41] ASTM International, Standard test method for compressive strength of cylindrical concrete specimens (C39/C39M-16), Pennsylvania, 2016.

[42] Ministry of Industry and Information Technology of the People's Republic of China (MIIT), Standard test method for the mechanical properties of ductile fiber reinforced cementitious composite (JC/T 2461-2018), Building Industry Press, Beijing, China, 2018.

[43] Standardization Administration of the People's Republic of China, Metallic materials-Tensile testing-Part 1: Method of test at room temperature (GB/T 228.1-2010), Beijing, China, 2010.

[44] J.J. Poldon, N.A. Hoult, E.C. Bentz, Distributed sensing in large reinforced concrete shear test, ACI Struct. J. 116 (2019) 235–245, https://doi.org/10.14359/51716765.

[45] X. Shao, Y. Dai, X. He, H. Wang, G. Wu, Real-time digital image correlation for quasi-static test in civil engineering, Acta Opt. Sin. 35 (2015) 1012003, https://doi.org/10.3788/AOS201535.1012003.

[46] X. Xu, Y. Ma, X. Shao, X. He, C. Quan, Experimental verification of full-field accuracy in stereo-DIC based on the ESPI method, Appl. Opt. 61 (2022) 1539–1544, https://doi.org/10.1364/ao.451341.

[47] R. Park, T. Paulay, Reinforced concrete structures, John Wiley & Sons, Hoboken, NJ, 1975.

[48] Y. Huang, D. Gu, S. Mustafa, S. Grünewald, M. Luković, Shear behaviour of reinforced concrete beams strengthened with ultra-high performance fiber reinforced concrete (UHPFRC), Case Stud. Constr. Mater. 19 (2023) e02441, https://doi.org/10.1016/j.cscm.2023.e02441.

[49] J. Yao, C.K.Y. Leung, Scaling up modeling of strain-hardening cementitious composites based on beam theory: from single fiber to composite, Cem. Concr. Compos. 108 (2020) 103534, https://doi.org/10.1016/j.cemconcomp.2020.103534.

[50] C. Lu, C.K.Y. Leung, Theoretical evaluation of fiber orientation and its effects on mechanical properties in engineered cementitious composites (ECC) with various thicknesses, Cem. Concr. Res. 95 (2017) 240–246, https://doi.org/10.1016/j.cemconres.2017.02.024.

[51] Q. Liao, Y.R. Su, J.T. Yu, Q. yao Yao, D. Meng, K.Q. Yu, Experimental and theoretical investigation on compression-shear properties of high-strength engineered cementitious composites (HS-ECC), J. Build. Eng. 67 (2023) 106015, https://doi.org/10.1016/j.jobe.2023.106015.

[52] Q. Liao, Y. Su, J. Yu, K. Yu, Compression-shear performance and failure criteria of seawater sea-sand engineered cementitious composites with polyethylene fibers, Constr. Build. Mater. 345 (2022) 128386, https://doi.org/10.1016/j.conbuildmat.2022.128386.
[53] Z. Hu, Y. Zhou, B. Hu, X. Huang, M. Guo, Local use of ECC to simultaneously enhance the shear strength and deformability of RC beams, Constr. Build. Mater. 353 (2022) 129085, https://doi.org/10.1016/j.conbuildmat.2022.129085.
[54] K. F. Sarsam, M.M.S. Ridha, Z. H. Mahdi, Investigation of the dowel and friction forces in fiber reinforced ultra high performance concrete beams, Eng. Technol. J. 30 (16) (2012) 2923–2936, https://doi.org/10.30684/etj.30.16.14.
[55] A. Khazaee, M. Ghalehnovi, M. Rakhshanimehr, Experimental evaluation of dowel action in ultra-high performance concrete, Iran. J. Sci. Technol. - Trans. Civ. Eng. 46 (2) (2022) 1129–1140, https://doi.org/10.1007/s40996-021-00627-6.
[56] J. Xia, Y. Xiao, K.R. Mackie, M. Al-Ramahee, A. Mirmiran, Dowel action and shear strength contribution of high strength rebar embedded in ultra-high performance fiber reinforced concrete, Eng. Struct. 83 (2015) 223–232, https://doi.org/10.1016/j.engstruct.2014.11.004.
[57] Y. Yang, J. Walraven, J. den Uijl, Shear behavior of reinforced concrete beams without transverse reinforcement based on critical shear displacement, J. Struct. Eng. 143 (1) (2017) 04016146, https://doi.org/10.1061/(asce)st.1943-541x.0001608.